

Support-free speckle-correlation imaging with implicit neural representation

Felipe Guzmán,^a Ryoichi Horisaki,^b Esteban Vera,^{a,*}

^aSchool of Electrical Engineering, Pontificia Universidad Católica de Valparaíso, Valparaíso, Valparaíso, 2340000, Chile

^bGraduate School of Information Science and Technology, The University of Tokyo, Tokyo, 113-8656, Japan

Abstract. We present a method for imaging through unknown scattering media by combining speckle-correlation and implicit neural representation (INR). The approach uses multi-layer perceptrons to reconstruct objects from a single speckle pattern, guided by autocorrelation similarity, without requiring prior calibration or object knowledge. Instead of relying on fixed binary supports in conventional methods, our method effectively removes this constraint, as the INR learns an implicit spatial support directly from the data. Experimental results on fluorescent cell images show that this framework produces sharper reconstructions with fewer artifacts and more stable performance across varying object sizes. Compared to phase retrieval and deep image priors, our INR-based method achieves cleaner and more accurate results in a compact and calibration-free lensless imaging setup.

Keywords: implicit neural representation; speckle correlation imaging; memory effect; implicit neural representation.

*Esteban Vera, E-mail: esteban.vera@pucv.cl

1 Introduction

Imaging through scattering media presents a major challenge in optics and may lead to transformative applications if made possible. In biomedical imaging, it can enable imaging through tissue, even though scattered light crossing other internal structures produces blurred images^[1–3]. Similarly, it can also enable non-line-of-sight imaging, reconstructing hidden scenes from unintelligible wall reflections^[4–6]. Nevertheless, understanding and exploiting the statistical properties of the scattering medium have been crucial to advancing this imaging modality.

For weakly scattering media, methods that separate ballistic and scattered photons have been developed^[7–11]. However, solutions in highly scattering environments often involve complex hardware—such as wavefront sensors or guide stars^[12–14]—or invasive techniques^[15,16], which tend to be impractical. On the other hand, non-invasive alternatives such as speckle-correlation imaging exploit the memory effect. This simple yet effective technique has been applied to multidimensional imaging, where phase retrieval algorithms reconstruct the object solely from the autocorrelation of its speckle pattern^[17–22].

Recent advances in machine learning, particularly deep learning, have dramatically improved computational imaging applications^[23], providing new solutions to several inverse problems related to lensless imaging^[24] and phase retrieval^[25]. In imaging through scattering media, deep learning models have been used to map complex speckle patterns to images of hidden objects^[26,27]. However, these methods often rely on large datasets, which are difficult to obtain, or simulated data that may not necessarily match real-world scenarios. Recent work, such as in^[28], utilizes convolutional neural networks (CNNs) as deep image priors (DIP), allowing speckle-correlation imaging through extrapolation. Nonetheless, this method remains computationally expensive and requires fine-tuning and ad hoc regularizers for different objects. In general, most state-of-the-art methods rely on explicit support to confine the solution, imposing assumptions about the object’s size, which is, more than often, difficult to estimate in scattering environments^[29].

In recent years, multilayer perceptrons (MLPs) have been used as a universal approximation tool^[30], embedding signals in an implicit neural representation (INR). This approach efficiently represents complex signals with fewer layers and weights compared to convolutional networks. MLPs have been successfully applied to compress high-dimensional signals and solve inverse problems such as inpainting^[31] and Fourier ptychography^[32]. A recent study^[33] applies MLPs—under the scope of INRs—to represent images passing through scattering media, although it requires previous calibration of the point spread function (PSF) to integrate the forward model and minimize the loss function. To avoid the need for calibration or prior knowledge about the object or its support, herein we propose an innovative use of the INR with MLPs to reconstruct images passing through unknown scattering media. Next, we describe the

acquisition model and introduce the INR reconstruction model.

2 Methods

In traditional imaging systems, the object is represented as an intensity distribution $O(\mathbf{x})$ where \mathbf{x} is a vector of integers that represent the spatial coordinates; then the acquisition of the image in the detector plane $I(\mathbf{x})$ can be described as

$$I(\mathbf{x}) = O(\mathbf{x}) * h(\mathbf{x}) + n(\mathbf{x}), \quad (1)$$

where $h(\mathbf{x})$ is the impulse response of the system, which maps the object to the detector plane, $n(\mathbf{x})$ is the measurement noise, and $*$ represents the convolution operator. When we introduce a scattering medium between the object and the detector instead of a lens, as illustrated in Fig. 1a, then $h(\mathbf{x})$ models the scattering of light, leading to noisy, low-contrast speckle patterns instead of images of the scene at the detector plane, heavily degrading the spatial features of $O(\mathbf{x})$.

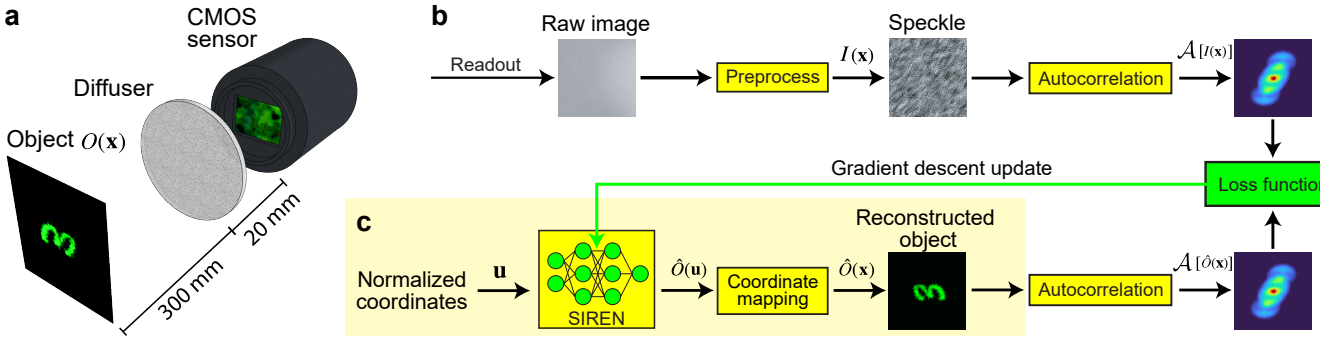


Figure 1: The proposed scheme for speckle-correlation imaging through implicit neural representation: **a** lensless experimental setup; **b** implicit neural representation training; **c** object reconstruction.

However, the autocorrelation of the recorded speckle retains striking similarities to the autocorrelation of the original object, a property that arises from the memory effect found in speckle-correlation^[17]. This isoplanatism, can be expressed as $\mathcal{A}[I(\mathbf{x})] \approx \mathcal{A}[O(\mathbf{x})]$, where $\mathcal{A}[\cdot]$ represents the autocorrelation operator. Prior art has exploited autocorrelation to reconstruct objects using techniques such as speckle-correlation imaging and phase retrieval, which demand previous knowledge of the object support to constrain the solution space. This becomes particularly problematic in highly scattering environments, where the true size of the object is uncertain, requiring a trial-and-error approach to infer the support.

On the other hand, INRs have emerged as a promising alternative offering sampling flexibility. Originally developed for compression, INRs have recently been adapted for computational imaging enabling a continuous and flexible representation of objects without the constraints imposed by discretization. Although early efforts used MLPs with Rectified Linear Unit (ReLU) as the activation function for direct imaging, recent advances have shown that alternative activation functions, such as $\sin(\cdot)$, deliver better signal expression, especially when capturing high-frequency details in the image^[34]. Considering this, if we express the reconstructed object $\hat{O}(\mathbf{x})$ as a continuous signal, then it can be represented as

$$\hat{O}(\mathbf{u}) = \text{SIREN}(\mathbf{u}), \quad (2)$$

where the function $\text{SIREN}(\cdot)$ represents the forward operation of the MLPs, while $\mathbf{u} \in [-1, 1]^{N^2 \times 2}$ is a vector of normalized coordinates. This normalization by N samples, is a technical requirement for the SIREN architecture, as it keeps inputs within the periodic $\sin(\cdot)$ activation function. This approach uses MLPs for INRs to correlate all the information content of the signal without the constraints of fixed kernel sizes—typical in traditional CNNs—while maintaining constant computational complexity. Moreover, unlike conventional methods that require an explicit, the proposed method learns its own support implicitly, eliminating the need for an explicit mask. The autocorrelation loss guides the optimization to map background coordinates to zero. This process results in a support-free reconstruction, revealing the true boundaries of the object.

As illustrated in Fig. 1b, the input image is first preprocessed to enhance speckle contrast. This involves offset removal, followed by element-wise division between the image and its low-pass filtered version. A cropping step is also applied to mitigate edge artifacts from the convolution. The object is then represented by an MLP, which maps 2D

spatial coordinates \mathbf{u} to intensity values $\hat{O}(\mathbf{u})$. Querying this implicit model over a rescaled coordinate grid \mathbf{x} yields an image at the desired resolution, as shown in the reconstruction subroutine in Fig. 1c. The error is computed by comparing the autocorrelation of the measured speckle pattern with that of the reconstructed object, and is used to update the MLP weights. In this study, we use the following loss functions, where MSE is the mean-square-error and SSIM the structural-similarity-index.

$$\text{Loss}_1 = \text{MSE} \left(\mathcal{A} [I(\mathbf{x})], \mathcal{A} [\hat{O}(\mathbf{x})] \right) \quad (3)$$

$$\text{Loss}_2 = 1 - \text{SSIM} \left(\mathcal{A} [I(\mathbf{x})], \mathcal{A} [\hat{O}(\mathbf{x})] \right). \quad (4)$$

3 Experimental results

The measured speckle autocorrelation inherently contains experimental noise. A significant drawback of using a standard MSE loss is that it forces the network to overfit this noise, which in turn creates artifacts in the reconstructed object. In contrast, the SSIM loss function in Eq. (4) optimizes for structural similarity rather than pixel-wise fidelity. This characteristic allows the network to effectively ignore non-structural noise present in the target autocorrelation. Consequently, the INR-SSIM method converges to a cleaner solution that better represents the true object autocorrelation, obtaining a more faithful reconstruction. Although other works^[35–37] have reported superior results by combining SSIM and L2 loss for other inverse problems, our testing revealed no significant improvement from such a combination compared to using SSIM alone.

We label the two versions of the proposed method as INR-MSE and INR-SSIM, accordingly. The experimental setup is illustrated in Fig. 1a, consisting as a lensless imaging system, where a glass diffuser is used as a scattering medium, and an OLED screen of a Samsung S8 Ultra tablet to project 2 cm objects. The images are captured using a QHY600M cooled camera, loaded with a SONY IMX455 CMOS sensor, a 60-megapixel, 16-bit, backside-illuminated device with 2×2 binning to boost sensitivity in low-light conditions.

The OLED was placed 300 mm from the diffuser, and the diffuser 20 mm from the sensor. The exposure time was set between 10 to 30 seconds depending on the object brightness. After standard preprocessing following the recommendations of^[20], the final speckle is cropped at 800×800 pixels.

The INR of choice was the SIREN model^[34], implemented as an MLP with a two-neuron input layer, three hidden layers of 128 neurons using sine activations, and a single output neuron with a sigmoid activation function to constrain intensity values. The network’s learnable parameters are optimized using ADAM with an initial learning rate of 10^{-3} , which decays by a factor of 0.98 every 100 iterations over a total of 8,000 iterations. On an RTX 3050, each full-image forward pass takes ~ 5 ms and the network converges in ~ 47 s. Once trained, the MLP itself encodes the high-resolution object, enabling efficient storage and reconstruction by simple coordinate queries.

Figure 2 displays five objects of increasing complexity. The first object—a simple letter “V”—serves as a baseline, while objects 2 to 5 are cells from the publicly available SR-CACO-2 fluorescence microscopy dataset^[38]. For each object, we compare four reconstruction methods: hybrid input output (HIO) (following the recommendations of Ref.^[19]), the use of deep image prior as an image regularizer (DIP), and the two versions of the proposed technique INR-MSE and INR-SSIM. During the reconstruction process using HIO and DIP, we enforced a 200×200 pixels support to constrain the solution space within the expected size of the objects. For our method variants, the reconstructions were cropped from 800×800 pixels down to a 200×200 pixels region of interest. For all methods, we performed corrections to resolve any flipping or shifting ambiguities. For each object we perform 100 runs and select the best for visual inspection.

By examining row **b** in Fig. 2, we see that the HIO algorithm recovers the general shape of the object but omits several structural details. Moreover, the reconstructed intensity is concentrated into just a few pixels, so when displayed as an 8-bit image, large portions of the object appear completely black. Analyzing the first object in Fig. 2 reveals that all other methods successfully reconstruct the letter. However, the use of DIP produces a thinner, curved letter. In contrast, INR-MSE preserves the original thickness of the letter, while introducing background noise and diminishing the overall quality. Finally, INR-SSIM delivers better matched thickness and minimal artifacts, despite delivering rounded corners. When inspecting the second object, we observe a circular-shaped cell cluster, or spheroid, with individual cells forming its perimeter. With DIP, the overall spheroid shape is reconstructed, but the cell thicknesses deviate from the reference. On the other hand, INR-MSE produces more accurate thicknesses but introduces noticeable intensity saturation, making it difficult to resolve individual cells. In contrast, INR-SSIM presents a smoother intensity distribution and delivers clear resolution of most cells, although two of them appear merged. The third column of Fig. 2 shows a wider sample containing multiple spheroids and isolated point-source cells. DIP fails to reconstruct several cells, while INR-MSE introduces noise that could be mistaken for additional cells. On the contrary, INR-SSIM achieves the best balance between object clarity and resolution of spheroids and

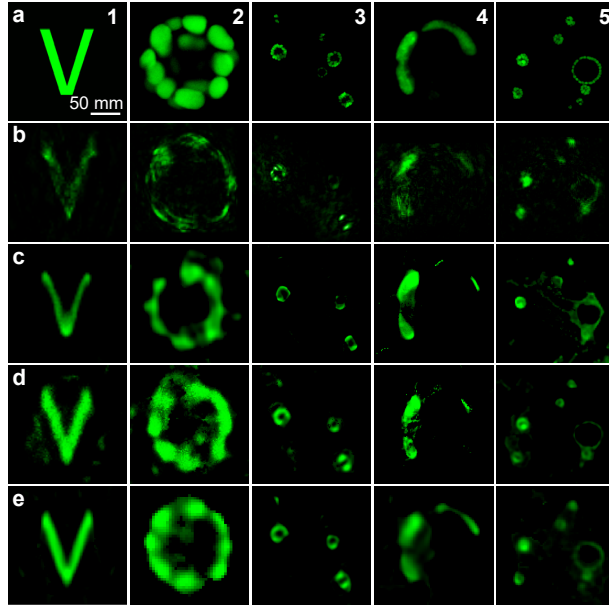


Figure 2: Experimental results. **a** object projected on the OLED screen. **b** reconstruction without priors with 200×200 support, **c** reconstruction with DIP with a 200×200 support, **d** INR-MSE with a 800×800 upper bound, and **e** INR-SSIM with a 800×800 upper bound.

individual cells. However, none of the methods successfully reconstruct the faintest spheroid in the reference. The fourth object exhibits similar behavior to column two, where INR-MSE struggles from intensity saturation, while INR-SSIM provides the most faithful reconstruction. Finally, the most challenging object is shown in the fifth column of Fig.2, clearly demonstrating the limitations of the DIP method in producing a coherent reconstruction. Although INR-MSE is able to improve shape accuracy, it suffers from noise-related artifacts. In contrast, INR-SSIM yields the cleanest reconstruction of both the large spheroid and the smaller structures.

Quantitatively, each method is compared with the object projected on the OLED screen and several metrics were calculated, from the traditional SSIM and PSNR but also using Learned Perceptual Image Patch Similarity (LPIPS) [39] and Multi Scale SSIM (MS-SSIM) [40]. To correct for spatial shift, which can artificially penalize pixel-sensitive metrics, a flip and shift compensation was first performed. Subsequently, each metric was computed exclusively on the region of interest for each object.

Table 1: Mean metrics (averaged across all objects) per reconstruction method. Arrows indicate whether higher (\uparrow) or lower (\downarrow) values represent better quality.

Method	LPIPS \downarrow	SSIM \uparrow	MS-SSIM \uparrow	PSNR [dB] \uparrow
HIO	0.17 ± 0.05	0.84 ± 0.03	0.85 ± 0.05	22.42 ± 5.77
DIP	0.12 ± 0.03	0.88 ± 0.05	0.86 ± 0.04	21.41 ± 4.00
INR-MSE	0.13 ± 0.04	0.89 ± 0.05	0.90 ± 0.02	23.04 ± 4.03
INR-SSIM	0.10 ± 0.02	0.90 ± 0.03	0.92 ± 0.03	24.28 ± 2.49

Based on the averaged results presented in Table 1, INR-SSIM is the superior method across all four quality metrics. It exhibits the optimal performance with the lowest LPIPS (0.10), signifying the highest perceptual similarity. Concurrently, it yields the highest scores for structural metrics, specifically SSIM (0.90) and MS-SSIM (0.92). Furthermore, INR-SSIM achieves the highest PSNR (24.28), indicating the lowest pixel-level error, although the sensitivity of this metric to pixel shifts should be noted. Other methodologies display performance trade-offs; for instance, DIP offers competitive LPIPS and SSIM scores but yields the lowest average PSNR (21.41). The HIO baseline is consistently outperformed by all compared methods. Further analysis is presented in Table S1 of the supplementary document.

Figure 3 displays the autocorrelation of object 5 in Fig.2. When comparing the autocorrelation of the digital ground-truth object in Fig. 3a with the one generated from the captured (and preprocessed) speckle pattern in Fig. 3b, we notice clear differences in the sharpness of the features, most likely due to imperfections in the display and acquisition process, plus deviations of the scattering media from an ideal one. Figure 3c shows the results using

INR-MSE, being almost identical to the autocorrelation from the speckle pattern shown in Fig. 3b. On the other hand, when using INR-SSIM (displayed in Fig. 3d), the autocorrelation exhibits a sharper structure that more closely resembles the autocorrelation of the original, unobstructed object.

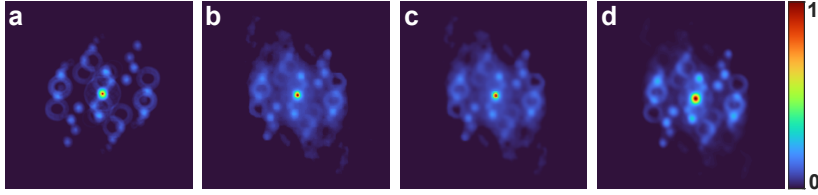


Figure 3: Normalized autocorrelation of object 5 from Fig. 2 computed from the: **a** true OLED object, **b** speckle pattern after preprocessing, **c** INR-MSE and **d** INR-SSIM. The pixel count is cropped to 700×700 for visualization purposes.

Most speckle-correlation imaging algorithms require the previous definition of a support mask in the reconstruction process. For instance, both HIO and DIP deliver reasonable results when a support mask is applied, as shown in Fig. 3. However, this can be problematic in scattering environments, where accurately estimating the size of the object beforehand is extremely difficult. In Fig. 4 we show the outputs obtained for object 5 when using different reconstruction techniques without cropping or support masks, where neither HIO (Fig. 4a) nor DIP (Fig. 4b) are able to reconstruct the underlying objects. In contrast, in the proposed INR method we imposed an 800×800 pixels upper bound limit on the coordinate system (way larger than the real support of the objects), enabling the MLP to automatically discover the boundaries of the object, as shown in Fig. 4c, which can be cropped later to create the result in Fig. 3. However, please note that the final size tends to vary around 5 pixels depending on MLP initializations and can appear in other positions within the domain, due to the position invariance property of the autocorrelation.

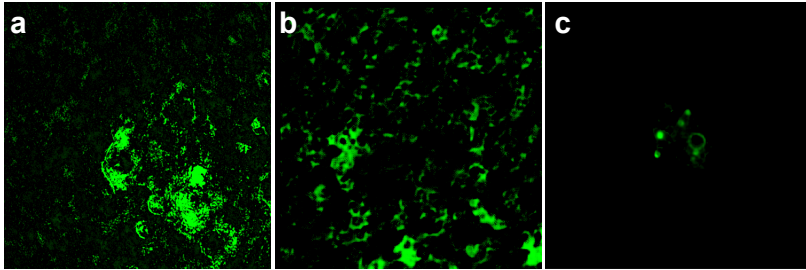


Figure 4: Reconstruction results of object 5 from Figure 3 without support. **a** HIO; **b** DIP; **c** INR-MSE.

Table 2 presents the success rate for all evaluated methods, considering a 200×200 support for HIO and DIP. Success was determined quantitatively. First, reconstructions were algorithmically corrected for pixel shift and 180° flip ambiguities by maximizing their cross-correlation with the ground truth. Second, a run was marked as successful if a computed evaluation metric on the corrected reconstruction with more of a 12 dB of PSNR. The highest success rate is obtained with INR-MSE, although its reconstructions often contain noise around the object. On the other hand, INR-SSIM produces cleaner and more stable results with minimal background noise, despite a slightly lower success rate. Notably, INR-SSIM produces consistent outputs across different runs, all converging to the same object shape without significant variation. Overall, both methods are suitable for different scenarios: INR-MSE is preferable when minimizing the risk of failure is important, while INR-SSIM is more appropriate when reconstruction precision and stability are the main goals.

Table 2: Success rates for all experimental runs. Determined by compensating for pixel shift and flip and high metric thresholding.

Test runs	HIO	DIP	INR-MSE	INR-SSIM
Success	307	290	389	285
Failure	193	210	111	215
Success rate [%]	61.4	58.0	77.8	57.0

Further ablation studies, detailed in the supplementary document, investigated the impact of MLP architecture

(depth and width) and activation functions. For the objects tested, results indicate an optimal architecture of four layers with 128 neurons each. Our findings regarding activation functions align with Sitzmann *et al.*^[34], confirming the superiority of periodic activations for this application.

The proposed method has practical constraints for dynamic scenarios. First, our implementation uses long exposures (10–30 s), which is viable only for static media. Dynamic media, such as biological tissue, decorrelate within milliseconds^[41]. Exposures exceeding this time erase the speckle contrast required for reconstruction^[42]. This is a hardware limitation, not an algorithmic one; *in vivo* applications would require high-speed acquisition (>10,000 fps).

Second, the flip/shift ambiguities inherent to autocorrelation become critical. Independent frame reconstruction in a video may introduce random shifts or 180° flips, disrupting temporal coherence. Future work requires addressing these issues, likely via cross-frame correlation compensation and spatio-temporal regularization.

4 Conclusion

In summary, we presented an efficient method for reconstructing objects through scattering media, combining speckle-correlation imaging with implicit neural representation powered by multi-layer perceptrons. The results of our experiments show that the proposed method can successfully reconstruct cellular objects from scattered light, producing high-quality reconstructions from a single shot. Unlike traditional methods that require extensive calibration or large training datasets, our approach solely relies on the autocorrelation of the measured data, which simplifies the process and reduces computational burden. Additionally, our method can work without making any assumption regarding the object size since the MLP can implicitly create its own support. Minimizing the autocorrelation error introduces similar challenges to traditional speckle-correlation imaging, such as image shifting and flipping. These ambiguities arise from the autocorrelation invariance and barely hinder the overall accuracy. Finally, the use of SSIM instead of MSE in the loss function allowed the method to improve the results, despite diminishing the exceptional success rate provided by MSE, relaxing the reconstructed autocorrelation which finally resembles even better the original one. In conclusion, the proposed method represents a significant advancement in noninvasive, lensless imaging through scattering media without requiring prior knowledge of the object support, leading to promising applications in biomedical imaging and remote sensing.

Moving forward, future work could focus on extending this method to multidimensional imaging, including video and color, for instance. This can be achieved by expanding the coordinate system to incorporate wavelength or temporal dimensions, or both^[33]. However, enhancements in the sensing strategy are necessary to successfully decouple data along each dimension—for example, by using coded apertures. In addition, the use of additional priors such as the decay factor of the scattering medium, may facilitate the extension of the field-of-view^[28].

Disclosures

The authors declare no conflicts of interest.

Acknowledgments

Agencia Nacional de Investigación y Desarrollo (ANILLO ATE220022); Fondo Nacional de Desarrollo Científico y Tecnológico (EXPLORACION 13220234); Japan Society for the Promotion of Science (JP20H05890, JP23K26567, JP23H05444); Japan Science and Technology Agency (JPMJFR2448, JPMJAN25F1); Asahi Glass Foundation; SECOM Science and Technology Foundation.

References

1. H. Yu, J. Park, K. Lee, J. Yoon, K. Kim, S. Lee, and Y. Park, “Recent advances in wavefront shaping techniques for biomedical applications,” *Current Applied Physics* **15**(5), pp. 632–641, 2015.
2. S. Yoon, M. Kim, M. Jang, Y. Choi, W. Choi, S. Kang, and W. Choi, “Deep optical imaging within complex scattering media,” *Nature Reviews Physics* **2**(3), pp. 141–158, 2020.
3. A. R. Kherlopian, T. Song, Q. Duan, M. A. Neimark, M. J. Po, J. K. Gohagan, and A. F. Laine, “A review of imaging techniques for systems biology,” *BMC systems biology* **2**, pp. 1–18, 2008.
4. X. Liu, J. Wang, L. Xiao, Z. Shi, X. Fu, and L. Qiu, “Non-line-of-sight imaging with arbitrary illumination and detection pattern,” *Nature Communications* **14**(1), p. 3230, 2023.

5. A. Velten, T. Willwacher, O. Gupta, A. Veeraraghavan, M. G. Bawendi, and R. Raskar, "Recovering three-dimensional shape around a corner using ultrafast time-of-flight imaging," *Nature communications* **3**(1), p. 745, 2012.
6. M. O'Toole, D. B. Lindell, and G. Wetzstein, "Confocal non-line-of-sight imaging based on the light-cone transform," *Nature* **555**(7696), pp. 338–341, 2018.
7. A. P. Gibson, J. C. Hebden, and S. R. Arridge, "Recent advances in diffuse optical imaging," *Physics in medicine & biology* **50**(4), p. R1, 2005.
8. G. Anderson, F. Liu, and R. Alfano, "Microscope imaging through highly scattering media," *Optics letters* **19**(13), pp. 981–983, 1994.
9. P. Dean, M. Dickinson, and D. West, "Full-field coherence-gated holographic imaging through scattering media using a photorefractive polymer composite device," *Applied Physics Letters* **85**(3), pp. 363–365, 2004.
10. J. Guan, Y. Cheng, and G. Chang, "Time-domain polarization difference imaging of objects in turbid water," *Optics Communications* **391**, pp. 82–87, 2017.
11. S. Kang, S. Jeong, W. Choi, H. Ko, T. D. Yang, J. H. Joo, J.-S. Lee, Y.-S. Lim, Q.-H. Park, and W. Choi, "Imaging deep within a scattering medium using collective accumulation of single-scattered waves," *Nature Photonics* **9**(4), pp. 253–258, 2015.
12. M. J. Booth, "Adaptive optics in microscopy," *Philosophical Transactions of the Royal Society A: Mathematical, Physical and Engineering Sciences* **365**(1861), pp. 2829–2843, 2007.
13. R. Davies and M. Kasper, "Adaptive optics for astronomy," *Annual Review of Astronomy and Astrophysics* **50**(1), pp. 305–351, 2012.
14. R. Horstmeyer, H. Ruan, and C. Yang, "Guidestar-assisted wavefront-shaping methods for focusing light into biological tissue," *Nature photonics* **9**(9), pp. 563–571, 2015.
15. J. Schneider and C. M. Aegerter, "Guide star based deconvolution for imaging behind turbid media," *Journal of the European Optical Society-Rapid Publications* **14**(1), p. 21, 2018.
16. S. Yoon, S. Y. Cheon, S. Park, D. Lee, Y. Lee, S. Han, M. Kim, and H. Koo, "Recent advances in optical imaging through deep tissue: Imaging probes and techniques," *Biomaterials Research* **26**(1), p. 57, 2022.
17. I. Freund, M. Rosenbluh, and S. Feng, "Memory effects in propagation of optical waves through disordered media," *Physical review letters* **61**(20), p. 2328, 1988.
18. I. Freund, "Looking through walls and around corners," *Physica A: Statistical Mechanics and its Applications* **168**(1), pp. 49–65, 1990.
19. J. Bertolotti, E. G. Van Putten, C. Blum, A. Lagendijk, W. L. Vos, and A. P. Mosk, "Non-invasive imaging through opaque scattering layers," *Nature* **491**(7423), pp. 232–234, 2012.
20. O. Katz, P. Heidmann, M. Fink, and S. Gigan, "Non-invasive single-shot imaging through scattering layers and around corners via speckle correlations," *Nature photonics* **8**(10), pp. 784–790, 2014.
21. Y. Endo, J. Tanida, M. Naruse, and R. Horisaki, "Extrapolated speckle-correlation imaging," *Intelligent Computing* **2022**, 2022.
22. D. Wang, S. K. Sahoo, X. Zhu, G. Adamo, and C. Dang, "Non-invasive super-resolution imaging through dynamic scattering media," *Nature communications* **12**(1), p. 3150, 2021.
23. G. Barbastathis, A. Ozcan, and G. Situ, "On the use of deep learning for computational imaging," *Optica* **6**(8), pp. 921–943, 2019.
24. H. Kim, G. Song, J.-i. You, C. Lee, and M. Jang, "Deep learning for lensless imaging," *Journal of the Korean Physical Society* **81**(6), pp. 570–579, 2022.
25. K. Wang, L. Song, C. Wang, Z. Ren, G. Zhao, J. Dou, J. Di, G. Barbastathis, R. Zhou, J. Zhao, *et al.*, "On the use of deep learning for phase recovery," *Light: Science & Applications* **13**(1), p. 4, 2024.

26. R. Horisaki, R. Takagi, and J. Tanida, "Learning-based imaging through scattering media," *Optics express* **24**(13), pp. 13738–13743, 2016.
27. Y. Li, Y. Xue, and L. Tian, "Deep speckle correlation: a deep learning approach toward scalable imaging through scattering media," *Optica* **5**(10), pp. 1181–1190, 2018.
28. R. Mashiko, J. Tanida, M. Naruse, and R. Horisaki, "Extrapolated speckle-correlation imaging with an untrained deep neural network," *Appl. Opt.* **62**, pp. 8327–8333, Nov 2023.
29. M. Liao, D. Lu, W. He, G. Pedrini, W. Osten, and X. Peng, "Improving reconstruction of speckle correlation imaging by using a modified phase retrieval algorithm with the number of nonzero-pixels constraint," *Applied Optics* **58**(2), pp. 473–478, 2019.
30. K. Hornik, M. Stinchcombe, and H. White, "Multilayer feedforward networks are universal approximators," *Neural networks* **2**(5), pp. 359–366, 1989.
31. Z. Li, H. Wang, and D. Meng, "Regularize implicit neural representation by itself," in *Proceedings of the IEEE/CVF Conference on Computer Vision and Pattern Recognition*, pp. 10280–10288, 2023.
32. H. Zhou, B. Y. Feng, H. Guo, S. Lin, M. Liang, C. A. Metzler, and C. Yang, "Fourier ptychographic microscopy image stack reconstruction using implicit neural representations," *Optica* **10**(12), pp. 1679–1687, 2023.
33. T. Chien, R. Cao, F. L. Liu, L. A. Kabuli, and L. Waller, "Space-time reconstruction for lensless imaging using implicit neural representations," *Optics Express* **32**(20), pp. 35725–35732, 2024.
34. V. Sitzmann, J. Martel, A. Bergman, D. Lindell, and G. Wetzstein, "Implicit neural representations with periodic activation functions," *Advances in neural information processing systems* **33**, pp. 7462–7473, 2020.
35. A. Dudhane, H. Singh Aulakh, and S. Murala, "Ri-gan: An end-to-end network for single image haze removal," in *Proceedings of the IEEE/CVF conference on computer vision and pattern recognition workshops*, pp. 0–0, 2019.
36. L. Chen, X. Tian, S. Xiong, Y. Lei, and C. Ren, "Unsupervised blind image deblurring based on self-enhancement," in *Proceedings of the IEEE/CVF Conference on Computer Vision and Pattern Recognition*, pp. 25691–25700, 2024.
37. X. F. Ding, X. Duan, N. Li, Z. Khoz, F.-X. Wu, X. Chen, and N. Zhu, "Development of a deep learning method for phase retrieval image enhancement in phase contrast microcomputed tomography," *Journal of Microscopy* **299**, 2025.
38. S. Belharbi, M. Whitford, P. Hoang, S. Murtaza, L. McCaffrey, and E. Granger, "Sr-caco-2: A dataset for confocal fluorescence microscopy image super-resolution," in *NeurIPS*, 2024.
39. R. Zhang, P. Isola, A. A. Efros, E. Shechtman, and O. Wang, "The unreasonable effectiveness of deep features as a perceptual metric," in *Proceedings of the IEEE conference on computer vision and pattern recognition*, pp. 586–595, 2018.
40. Z. Wang, E. P. Simoncelli, and A. C. Bovik, "Multiscale structural similarity for image quality assessment," in *The thirty-seventh asilomar conference on signals, systems & computers, 2003*, **2**, pp. 1398–1402, Ieee, 2003.
41. M. M. Qureshi, J. Brake, H.-J. Jeon, H. Ruan, Y. Liu, A. M. Safi, T. J. Eom, C. Yang, and E. Chung, "In vivo study of optical speckle decorrelation time across depths in the mouse brain," *Biomedical optics express* **8**(11), pp. 4855–4864, 2017.
42. S. Zheng and J. Mertz, "Direct characterization of tissue dynamics with laser speckle contrast imaging," *Biomedical Optics Express* **13**(8), pp. 4118–4133, 2022.